Supporting Information for

Understanding instability in formamidinium lead halide perovskites: kinetics of transformative reactions at grain and sub-grain boundaries

Parth Raval[ǂ], Rhiannon M. Kennard[§], Eugenia S. Vasileiadou[#], Clayton J. Dahlman[§], Ioannis Spanopoulos,[# ¤] Michael L. Chabinyc[§], Mercouri Kanatzidis[#], and G. N. Manjunatha Reddy[#ǂ*]

[ǂ]*University of Lille, CNRS, Centrale Lille, Univ. Artois, UMR 8181- UCCS - Unité de Catalyse et Chimie du Solide, F-59000 Lille, France*
[§]*Materials Department, University of California, Santa Barbara, California 93106, U. S. A.*
[#] *Department of Chemistry, Northwestern University, Evanston, Illinois 60208, U. S. A.*

[¤]*Present address: Department of Chemistry, University of South Florida, Tampa, FL, 33620, U. S. A*

**Corresponding author: gnm.reddy@univ-lille.fr*

Table of contents

1. Materials and methods

Material synthesis. Large crystals (40-100 micrometers) of α-$FAPbI_3$ were synthesized following the synthetic protocol of the previous report by first preparing a solution of 8 mL of 57% w/w aqueous HI and 1.2 mL of 50% w/w aqueous H_3PO_2 and heating it to boiling during constant magnetic stirring in a fume hood.[1] 1137 mg (3 mmol) of lead acetate ($Pb[CH_3CO_2]_2 \cdot 3H_2O$) were dissolved in the solution until it became a clear yellow color. Then, 312 mg (3 mmol) of formamidine acetate ($FACH_3CO_2$) were added to the solution, forming yellow crystals. The reaction mixture was heated for an additional 30 minutes until all of the yellow crystals turned black. Before allowing the solution to cool, the hot yellow solution was carefully pipetted out of the container. The remaining black crystals in the mixture were quickly vacuum filtered and dried in a vacuum oven at 110 °C for 12h. It is noteworthy that the exposure of the black crystals to the solution at lower temperatures (e.g., allowing the mixture to cool before drying the crystals) caused the black crystals to partially convert back to the yellow crystal phase. Small crystals of α-$FAPbI_3$ were synthesized by adjusting the final annealing step. In this case, 1137 mg (3 mmol) of $Pb(CH_3CO_2)_2 \cdot 3H_2O$ were dissolved in a solution consisting of 8 mL of 57% w/w aqueous HI and 1.2 mL of 50% aqueous H_3PO_2, by heating to boiling whilst undergoing constant magnetic stirring. Then 312 mg (3 mmol) of formamidine acetate were added to the hot yellow solution, leading to the formation of yellow crystals (δ- phase) and black crystals (α-phase). They were collected by suction filtration and dried under vacuum at 180°C for 14h. This treatment gave rise to a stabilized black α-phase with a narrow distribution of particle sizes in the range of 20-40 micrometers. Yield: 1044 mg, (55% based on Pb)**.**

X-ray diffraction. X-ray diffraction patterns were acquired using an Empyrean Powder Diffractometer with a step size of 0.01313º, and a Cu-Kα source, operating with an accelerating voltage of 45 kV and the beam current of 40 mA, with samples rotated at 4 revolutions/min to improve signal-to-noise ratios. For high humidity *ex-situ* XRD experiments, powders of α-$FAPbI_3$ were placed in a small (4 mL) vial. This vial was placed in a larger (20 mL) vial containing water, such that the liquid water was not in direct contact with the powder. Then, the larger vial was capped with a Teflon-lined seal so that the relative humidity in this experiment was approximately 100%. To keep light out, we selected a large vial made of dark brown glass. For humidity tests (85% RH) with *ex-situ* powder XRD experiments, powder composition of fresh α-$FAPbI_3$ was suspended on glue placed on a zero-diffraction silicon substrate. This substrate was placed in a hydration chamber maintained at 85±2% RH (relative humidity in the air) in the presence of laboratory illumination. The substrate was taken out at regular intervals to acquire powder XRD patterns at a Rigaku MiniFlex powder diffractometer. All XRD measurements were carried out at room temperature.

Scanning electron microscopy (SEM) experiments were performed using an FEI Nova Nano 650 FEG SEM with beam currents of 0.40-0.80 nA, and at 7-10 keV accelerating voltage. Prior to SEM measurements, the samples were sputter-coated with gold to prevent charging.

Optical microscopy. All microscopy images were acquired with Leica S9i Digital Stereo Microscope, with a zoom range of 0.61x - 5.5x for a total magnification of 6.1x - 55x with 10x eyepieces. The microscope was integrated with a 10 M.P. camera to provide 1080P high-definition photographs of the perovskite particles. The perovskite particles (10-100 microns range) were dispersed on a glass slide, which was placed in a hydration chamber with 85% relative humidity in the air at room temperature. The glass slide was taken out from the hydration chamber at the indicated intervals to acquire micrographs, whereby the materials were exposed to moisture (45-60% RH) during the image collection. Photographs were acquired for the fresh black phase, intermediate black/yellow, and yellow phase at different magnifications for the small and large particles to be identified and distinguished.

Photoluminescence. For photoluminescence (PL) studies, fresh $FAPbI_3$ black phase and intermediate black/yellow and yellow $FAPbI_3$ materials (after exposure to moisture at 85% RH) were considered. All samples were measured using a Horiba LabRam Evolution high-resolution confocal Raman microscope spectrometer (600 g/mm diffraction grating) equipped with a diode continuous-wave laser (473 nm, 25 mW) and a Synapse charge-coupled device camera. The utilized power output of the laser source was filtered to 1% of the maximum power output.

Solid-state NMR spectroscopy. Fresh and moisture-aged $FAPbI_3$ and $FAPbBr_3$ materials were separately packed into air-tight and opaque 1.3 mm (outer diameter) zirconia rotors fitted with VESPEL® caps to ensure the material stability during NMR data acquisition. All solid-state MAS NMR experiments were conducted *ex-situ* either on a 21.1 T (^{1}H, 900 MHz) Bruker AVANCE-NEO or 18.8 T (^{1}H, 800 MHz) Bruker AVANCE NEO NMR spectrometer using a 1.3 mm H-X probehead. Unless specified, the MAS frequency was 50 kHz in all ssNMR experiments. 1D ^{1}H MAS NMR spectra were acquired by co-addition of 16 transients. The relaxation delays were set to 45 s, as determined from saturation recovery measurements and analyses, leading to the total experimental time of ~12 minutes each. For $FAPbI_3$, 1D ^{207}Pb experiments were carried out using a spin-echo sequence with 4096 co-added transients using a relaxation delay of 800 ms, leading to an overall experimental time of ~1h each, and for $FAPbBr_3$ 2048 co-added transients were co-added leading to an experimental time of ~30 minutes. 2D ^{1}H-^{1}H double-quantum(DQ)-single-quantum(SQ) NMR spectra were acquired using Back-to-Back (BaBa) sequence under fast MAS.[2–4] A rotor-synchronized t_1 increment of 20 μs was applied with a recoupling time of 40 μs, which corresponds to two rotor periods ($2\tau_r$). The indirect ^{1}H DQ dimension was acquired using 128 t_1 increments, each with 16 co-added transients, leading to an experimental time of ~25h. 2D ^{1}H-^{1}H spin diffusion NMR experiments were acquired using three-pulse noesy-like sequence with 1, 50, and 200 ms of mixing times.[5,6] A rotor-synchronized increment of 20 μs was applied to detect 400 t_1 increments, each with 2 scans, leading to an experimental time of ~9h each. The ^{1}H-detected 2D ^{1}H-^{207}Pb cross-polarization (CP) heteronuclear correlation (HETCOR) spectra were acquired with 28 t_1 increments, each with 800 co-added transients, using a recycle delay of 300 milliseconds, leading to a total experimental time of ~2h.[7,8] CP contact time was 5 ms. The ^{1}H experimental shift was calibrated with respect to neat TMS using adamantane as an external

reference (^{1}H resonance, 1.82 ppm). The experimental ^{207}Pb shifts were calibrated using $Pb(NO_3)_2$ as an external standard according to IUPAC recommendation.[9]

To understand the impact of particle size on moisture-induced degradation, the large and small $FAPbI_3$ particles are placed in a closely packed desiccator at a controlled humidity (85% RH), and the water vapor content is examined using a hygrometer placed inside the desiccator. To carry out 1D and 2D experiments, these particles are taken out from the desiccator at regular intervals and packed into air-tight 1.3 mm NMR rotors. For the controlled humidity (40% RH) exposure, the $FAPbI_3$ samples were placed in a desiccator along with silica beads which achieved the relative humidity of 40±5%. In all cases, the sample packing time was 3-5 mins at ambient humidity of ~45±5% RH, so that any material degradation during the packing process is negligible compared to several hours of exposure to moisture in desiccators.

For light illumination experiments, small $FAPbI_3$ particles (20-40 micrometer) are considered. The samples were placed in separate air-tight glass desiccators, one of which is exposed to laboratory illumination while the other is stored in the dark. These materials were separately packed into the 1.3 mm NMR rotors, and *ex-situ* ^{1}H MAS NMR experiments were carried out.

For ^{2}H ssNMR studies, the deuteration of FA^+ cations in α-$FAPbI_3$ was achieved by placing it in a dark humidity chamber at ambient temperature along with a saturated solution of KCl in D_2O. The sample was then packed into a 1.3 mm zirconia rotor for ^{1}H and ^{2}H NMR experiments. The static 1D ^{2}H NMR spectrum was acquired by co-adding 4096 transients. In FA^+ cations, only NH_2 sites are expected to be deuterated during the exposure to D_2O vapor. The percentage of isotopic ^{2}H labeling of -NH_2 sites was measured by integrating the ^{1}H signals of NH_2 sites and comparing it with the -CH signal of the FA cation. This procedure allows up to 70% of NH_2 sites in FA^+ cations to be deuterated (*vide infra*).

To understand the effect of $^{1}H \leftrightarrow ^{2}H$ isotopic exchange and ^{2}H NMR lineshapes of cubic perovskite (α) and non-perovskites (δ) phases, two different control experiments were carried out: First, an α-$FAPbBr_3$ phase was used as a control material for cubic phase because it does not undergo a phase transformation in the presence of moisture. $FAPbBr_3$ was stored in a dark humidity chamber with D_2O vapor for 48h at ambient temperature. The D_2O exposed $FAPbBr_3$ material was then packed into a 1.3 mm air-tight zirconia rotor. The static 1D ^{2}H NMR experiment was acquired by co-adding 8192 transients. The extent of deuteration was examined by carrying out a 1D ^{1}H MAS NMR spectrum for the same material, acquired by co-adding 4 transients. A deconvolution analysis leads to an estimation of the degree of deuteration, which was found to be 33% (i.e., ~33% of -NH_2 sites were deuterated). Second, a non-perovskite δ-$FAPbI_3$ material (obtained after exposure of α-$FAPbI_3$ material to 85% RH for over a week) was used as a control sample. The δ-$FAPbI_3$ material was then placed in the dark humidity chamber with D_2O vapor for 48h. A static 1D ^{2}H NMR spectrum of this material was acquired by co-adding 73728 transients. Deconvolution of 1D ^{1}H MAS NMR spectrum, acquired by co-adding 4 transients, suggests ~30% of deuteration. These two different control experiments aid the analysis of ^{2}H NMR lineshapes of fresh and moisture aged α-$FAPbI_3$ (target) materials.

2. Experimental and simulated X-ray diffraction patterns of α– and δ–$FAPbI_3$

The experimental and simulated X-ray diffraction powder patterns of α– and δ–$FAPbI_3$ are shown in **Figure S1**. The experimentally observed powder patterns are in agreement with the previously XRD results for alpha and delta $FAPbI_3$ phases, indicating the phase purity of the materials.[10,11] The XRD powder patterns are simulated on the basis of previously published crystal structures using of Mercury package.[12]

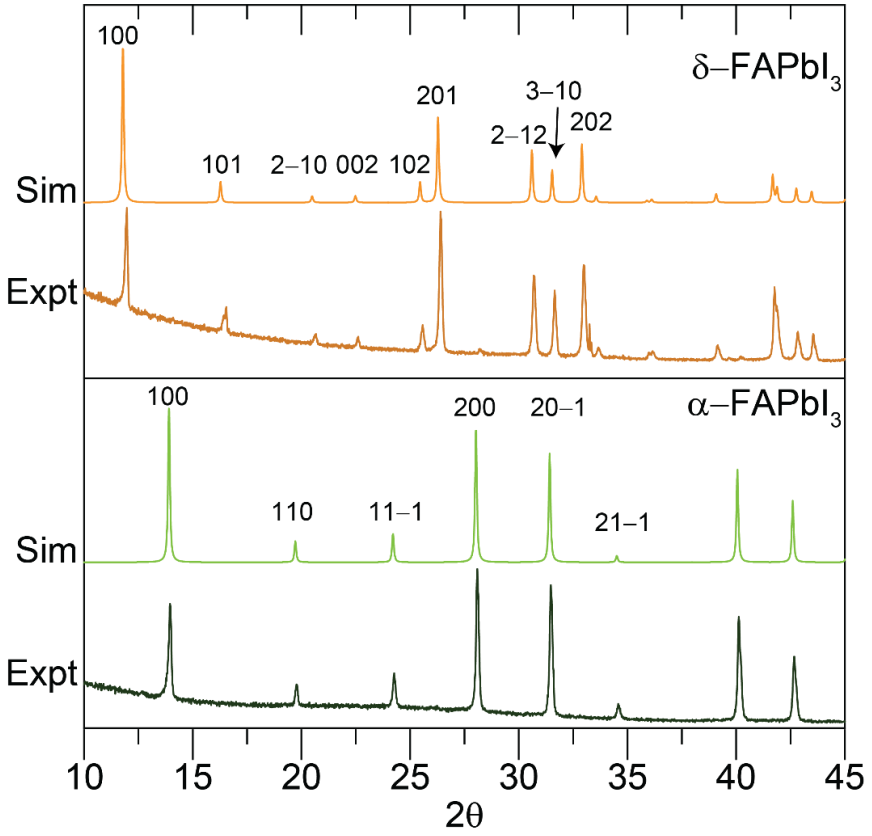

Figure S1. Experimental (Expt) and simulated (Sim) powder XRD patterns of α-$FAPbI_3$ and δ-$FAPbI_3$ acquired at room temperature.

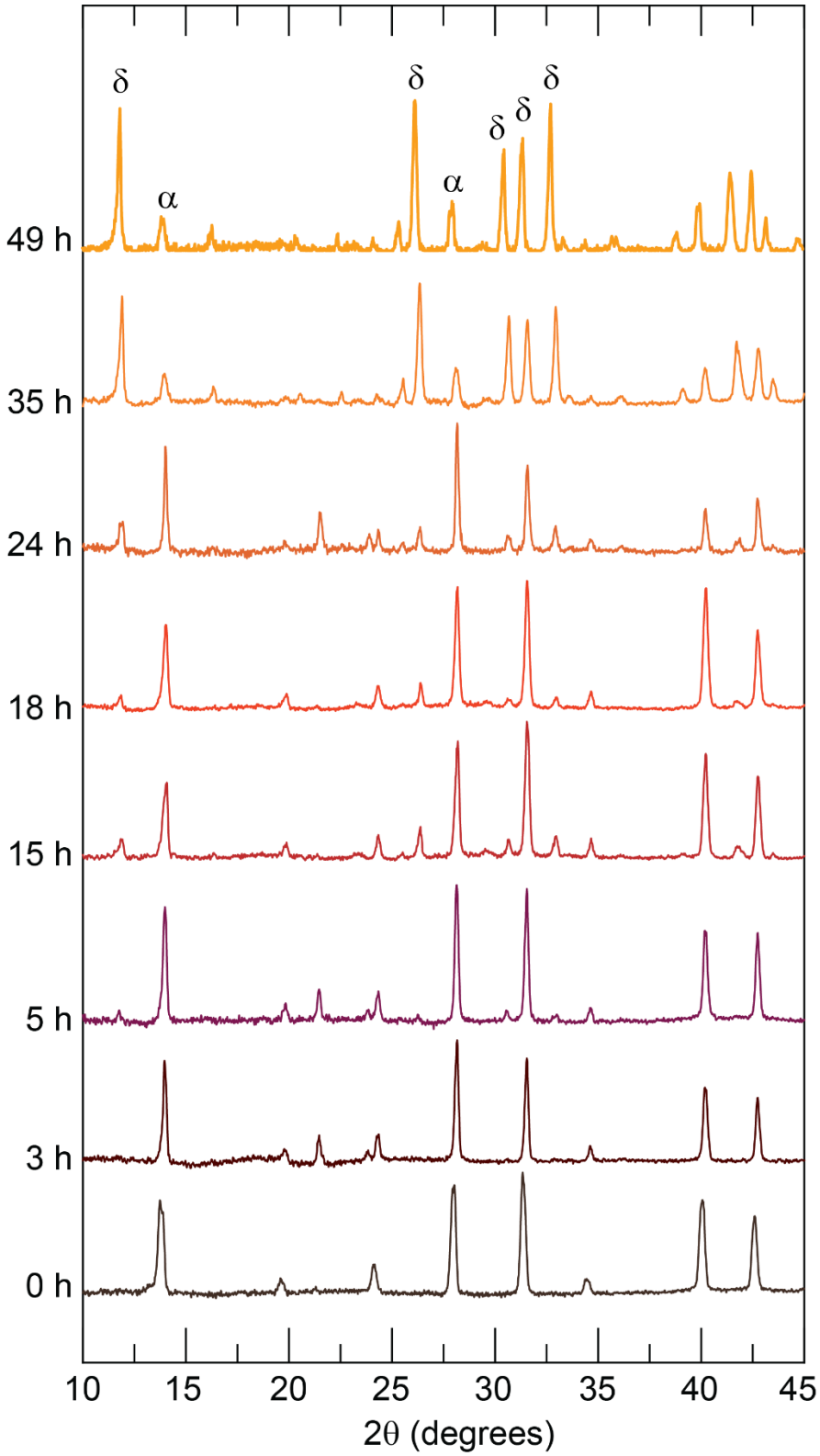

Figure S2. Powder XRD patterns of $FAPbI_3$ particles acquired before and after exposure to moisture at 85% RH for different durations as indicated.

3. SEM images of black $FAPbI_3$ phases with different particle sizes

The SEM images acquired for larger and smaller particle sizes are shown in Figure S3a and S3c, respectively. The acquired SEM images were then utilized to analyze particle size distribution for these particles synthesized with different annealing temperatures and time as mentioned in the synthetic protocol. ImageJ software was used to estimate the particle sizes observed in the SEM images. Based on this analysis, a histogram was generated, and fitted with Gaussian distribution function to extract the mean particle size and the standard deviation related to the particle size. The particle size distributions for small and large grains were found to be ≈32±11 μm and ≈74±41 μm, respectively.

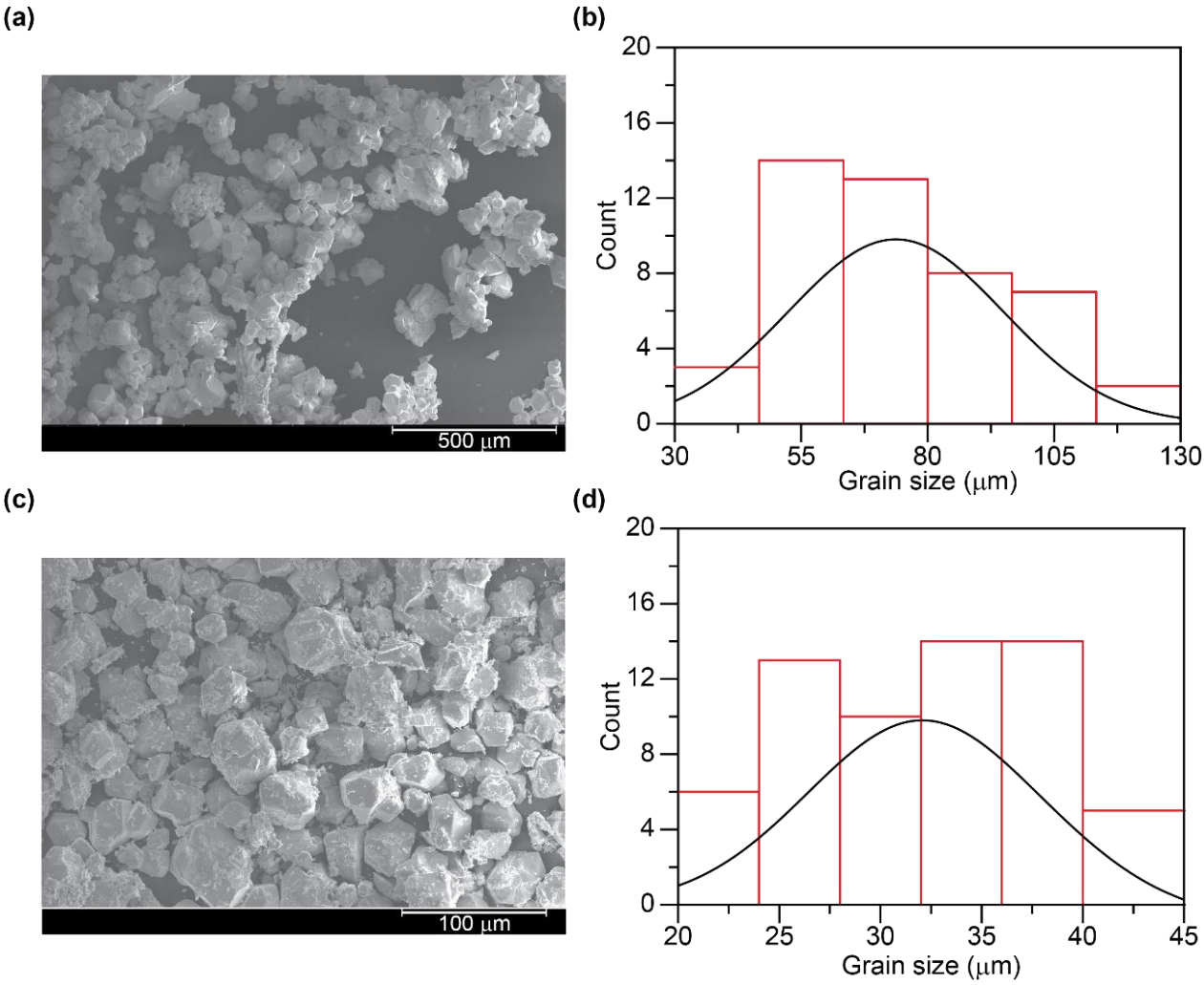

Figure S3. SEM images and particle-size distribution analyses of (a,b) large particles and (c,d) small particles, respectively.

4. High-resolution optical microscopy images of $FAPbI_3$

Figure S4 presents the optical micrographs of $FAPbI_3$ particles acquired before and after exposure to moisture, witnessing the morphological changes during the humidity induced degradation. For the fresh material (**S4a**, i.e., before exposure to moisture), the black feature indicates the cubic phase. Upon exposure to moisture (**S4b**: 3h, 85% RH), yellow features started to appear, particularly small black particles (<50 micrometers) tend to transfer to yellow phases much faster than the large particles (>50 micrometers), albeit to some heterogeneity in phase transformation of both large and small particles still exists. Upon further exposure to moisture to over 15h (**S4c**), black/yellow crystals have emerged. Of particular interest is the interface between the black and yellow phases at the grain and sub-grain boundaries. Much prolonged exposure of over 24h (**S4d**), the sizes of black particles that are trapped in the large yellow particles become smaller and smaller, indicating the sluggish phase transitions (**S4e,f**).

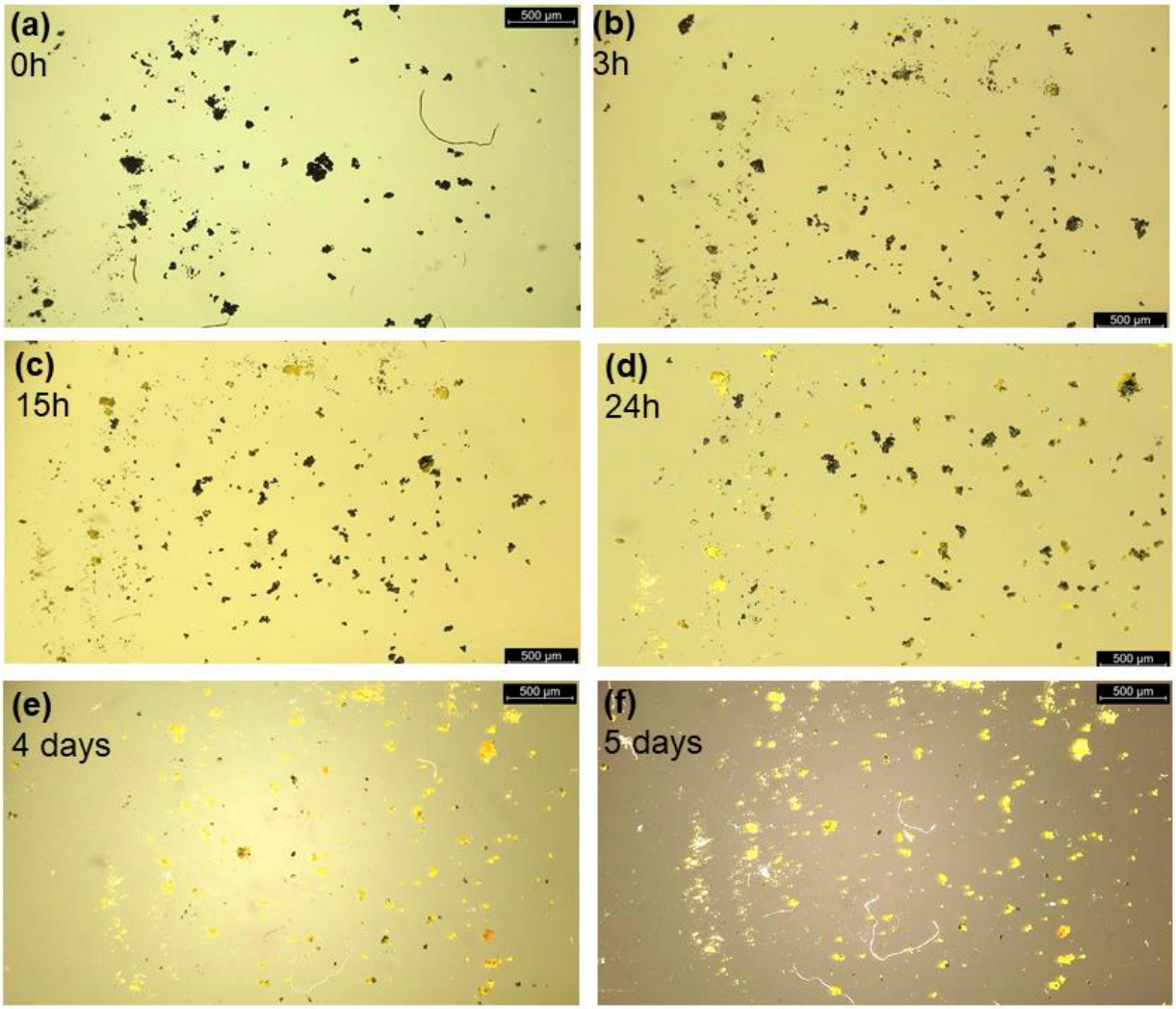

Figure S4. Optical microscopy images of $FAPbI_3$ particles dispersed on a glass plate obtained before and after exposure to moisture (*ex-situ* 85±5% RH): (a) fresh black phase, (b-c) after exposure to moisture after 3h, 15h, 24h, 4 days and 5 days.

A complete transformation from the black phase to the yellow phase predictably takes a week or even longer than a week. However, there is a small disparity in how fast different alpha $FAPbI_3$ particles convert to delta, as evidenced by optical microscopy analysis of different $FAPbI_3$ particle sizes and shapes. For example, a large particle (or cluster) on the top right of the images in **S4d,e** appears yellow, though many of the smaller particles appear black. To test this, we analyzed different particle sizes and compared. It was found that the rates of the transformative reactions were similar, which is due to the large overlap between the particle size distributions in the 10-100 microns range. Although the smaller particles do react slightly faster than the batch of larger particles, some large particles (or aggregates) in optical microscopy transform into the yellow phase faster than the small isolated particles. It can be hypothesized that this heterogeneity in reaction rates depends on the concentration of the surface and bulk defects and the extent of surface wettability (i.e., reactive inter- and intra-grain interfaces). For example, α-$FAPbI_3$ is known to have stacking fault defects that form δ-$FAPbI_3$, which could act as seeds for the phase transformation, and the concentration of these defects can vary with sample preparation.[13–15] Therefore, it would most likely to be required other methods of characterization - such as TEM (transmission electron microscopy) - in order to distinguish the contributions of surface area and buried reactive interfaces.

Further, we observed that the phase transformation occurs at lower rates after an initial rapid phase (i.e., after 15h of exposure to moisture). This slowing cannot solely be due to smaller particles reacting first, because some small particles are still black after many hours, contrary to what is seen for larger particles or aggregates in optical microscopy. Additional reasons for the slowing of the reaction could be that small α-$FAPbI_3$ particles are entrapped or buried under the large δ-$FAPbI_3$ particles, and/or that the δ-$FAPbI_3$ is less permeable to water. While optical microscopy analysis does not unambiguously indicate the existence of intermediate liquid-like transient species within the resolution capability of this technique, it shows that the phases remain segregated during the transformation reaction. The phase separation of black and yellow domains in partially transformed $FAPbI_3$ material observed via optical microscopy strengthens the interpretation of phase transition kinetics and the analysis of these $\alpha|\delta$–$FAPbI_3$ particles using more locally resolved techniques such as 2D solid-state NMR spectroscopy, as discussed in the later sections.

Figure S5 presents the high-resolution micrographs acquired before and after exposure to moisture for 10 days, whereby the changes in the morphological features of $FAPbI_3$ particles are monitored by inspecting specific particles depicted in solid and dashed circles (scale bars are shown in the figures insets). We observed that the closely proximate $FAPbI_3$ particles (sub-micron to a few microns distances) merge into large yellow crystals. For the large particle depicted in the solid circle, the black/yellow interfaces in the intermediate phase clearly depict that the nucleation of the yellow phase is non-uniform. As the phase transition progresses, the relatively small black particles trapped at the sub-surface layers of the large yellow particles transform at a slower rate into yellow crystals due to a lack of direct access to water molecules. Simultaneously, the surfaces of yellow particles become less hygroscopic (i.e., moisture resistant), which further impedes the

overall kinetics of the phase transition. Although analysis of micrographs provides specific insights into the phase transformation kinetics and visualization of the interface between black and yellow $FAPbI_3$ at macroscopic length scales, information on the atomic-scale intermolecular interactions between these two phases cannot be obtained by this technique. It explains, at least in part, how the rate of phase transitions exhibits a non-linear kinetic behavior, as will be discussed in the subsequent section using solid-state ^1H NMR kinetics studies and analyses.

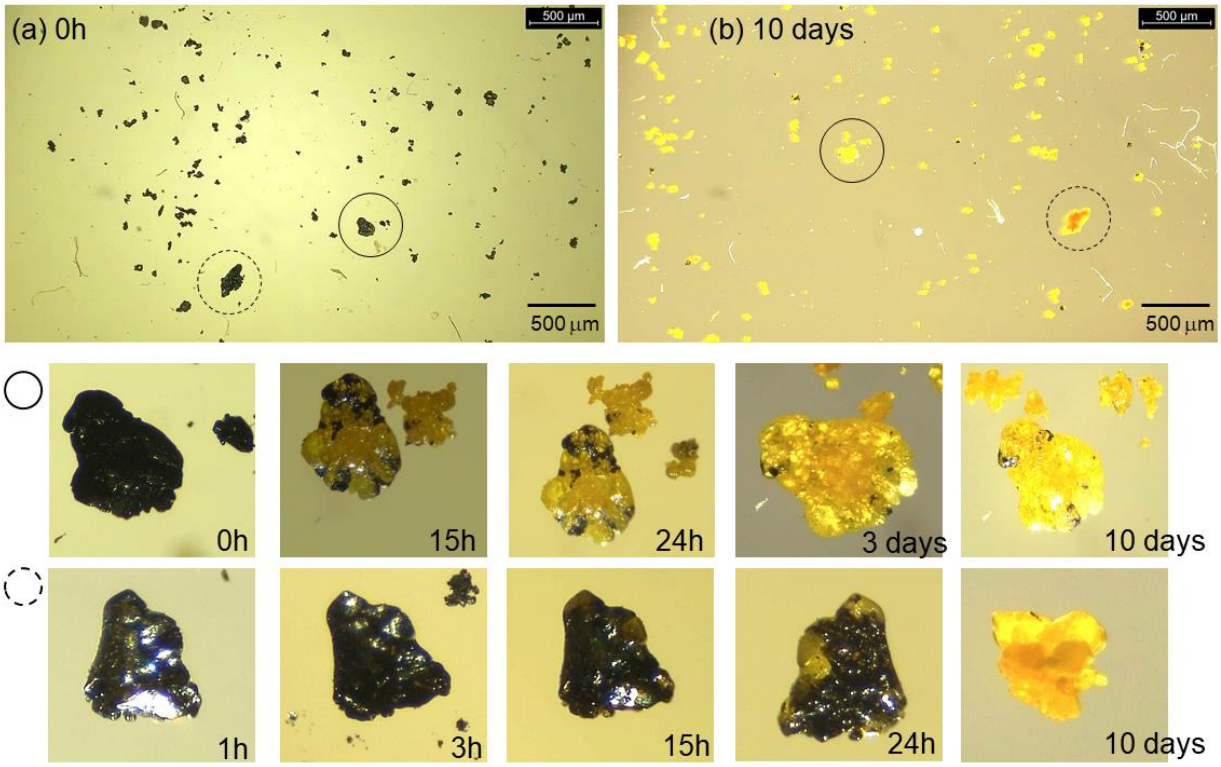

Figure S5. High-resolution optical microscopy images of $FAPbI_3$ particles (scale bars are given in the insets) dispersed on a glass plate obtained (a) before and (b) after exposure to moisture (*ex-situ* 85±5% RH): bottom panels depict the heterogeneous distribution of black and yellow microcrystals within the large particles as a function of moisture exposure time.

High-resolution micrographs of small particles as a function of moisture exposure time are displayed in **Figure S6**. During the early stage of hydration, nucleation of the yellow $FAPbI_3$ phase occurs at a much faster rate due to the high surface wettability and large surface area of the black particles (**S6a**) exposed to water molecules. After 3h of hydration (85% RH), the formation of traces of yellow particles was found (**S6b**), yet the large fraction of the grains appear to be black (**S5c**). After exposure to moisture for 24h (**S6d**), the majority of the material is then converted into the yellow phase, except minor regions of black particles entrapped in the yellow phase, which take much longer to convert to the yellow phase (**S6e-f**).

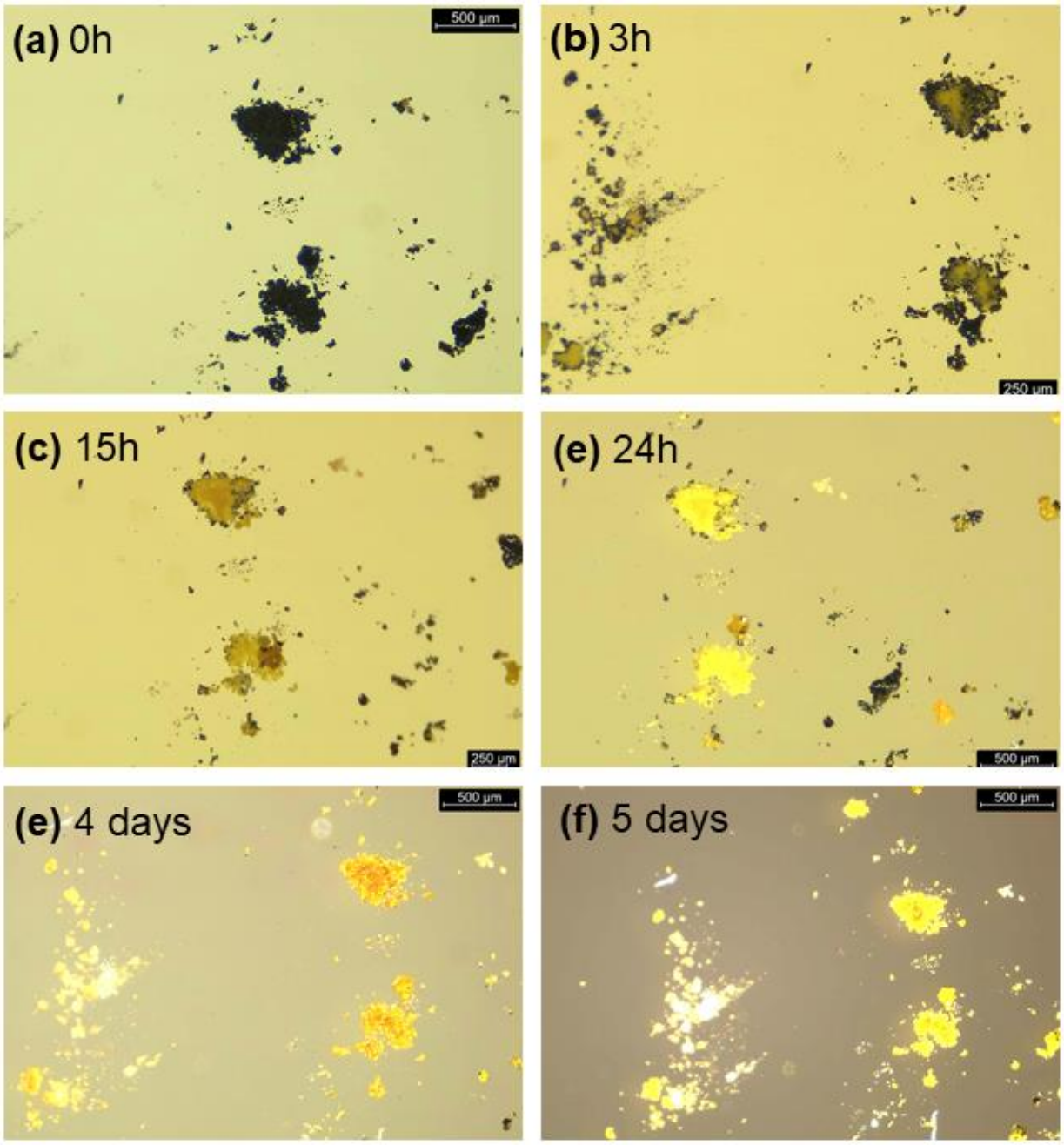

Figure S6. High-resolution optical microscopy images of small $FAPbI_3$ particles (scale bars are given in the insets) dispersed on a glass plate collected before and after exposure to moisture (*ex-situ* 85±5% RH): (a) fresh black phase, (b-c) after exposure to moisture after 3h, 15h, 24h, 4 days and 5 days. Although care was taken during the *ex-situ* analysis, some particles are displaced or several small black particles mingle together to form a large cluster of yellow particles due to mechanical shock when placing/removing the glass slide on an optical microscope and in a hydration chamber.

5. Kinetics of α→δ $FAPbI_3$ phase transformation reaction

In order to understand the kinetic behavior of the α→δ $FAPbI_3$ phase transformations, we plotted the ^1H signal intensity of -CH (FA^+) as a function of moisture exposure time. **Figure S7** compares kinetics plots, whereby normalized ^1H signal intensity (for zeroth order), natural logarithmic of normalized ^1H signal intensity (first-order/pseudo first-order), and inverse of normalized ^1H signal intensity (second-order) is plotted as a function of moisture exposure time. A good agreement between the experimental intensity (dots) and the fitted data (red line) was observed for the first-order kinetics with the co-efficient of determination R^2=0.995, while significant deviations are observed for both zeroth and second-order kinetics equations as indicated by R^2 in the range of 0.851-0.901. Although the surface area limited solid-state reactions are expected to follow the zeroth order rate law, this analysis suggests that the α→δ $FAPbI_3$ transformation reaction can be faithfully be modeled to the (pseudo)first-order reaction kinetics. The transformation follows the first-order, which depends on the concentration of the defect sites such as surface wetted $FAPbI_3$-H_2O and α|δ $FAPbI_3$ species at grain/sub-grain boundaries due to the surface dissolution. The rate increases as the concentration of water vapor increases or the particle exposure area increases.

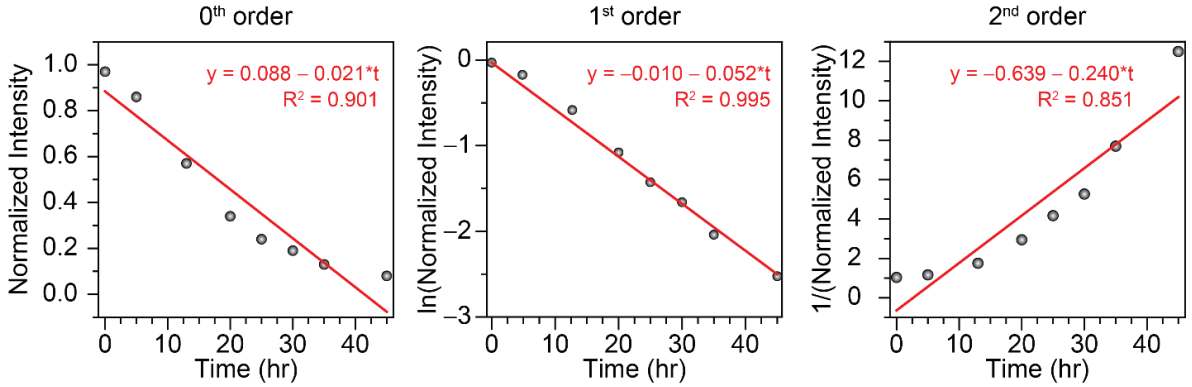

Figure S7. Normalized ^1H (-CH) signal intensity of FA cations in α-$FAPbI_3$ plotted as a function of moisture (85% RH in the air) exposure time.

To examine solid-state reaction kinetics, various models are reported in the literature: For example, Johnson-Mehl-Avrami-Kolmogorov (JMAK) model is often used to analyze phase transformation kinetics, which is described by the equation as: $y = 1 - \exp(-Bt^n)$, where y is the fraction of transformed phase, pre-factor B depends on nucleation rate of the homogeneously distributed particles, and *n* is Avrami exponent that depends on the dimensionality of the growth.[16–21] More sophisticated solid-state kinetic models have been reported.[22,23] It has also been shown that the Jander equation can model the kinetics of reactions in a powder form, which can be described as $k_t/R^2 = [1-(1-\alpha)^{(1/3)}]^2$ where k is a rate constant, t is time, R is the initial radius of a solid particle, and α is the fractional degree of reaction.[24,25] Some of these models postulate that the particles are spheres of the same size, which does not represent the $FAPbI_3$ particles used in this study. Although the defect concentration plays a crucial role in the α→δ $FAPbI_3$ transformation, disentangling surface and bulk defects (sizes and shapes, stacking faults) and expressing defect concentrations in terms of Kroger-Vink notation is also relatively less straightforward. To summarize, the (pseudo)first-order kinetics data presented in this study is more consistent with a solid-liquid-solid transition than a direct solid-to-solid transition, as corroborated by the analysis of ^2H NMR spectra (Figure 4 main text) and 2D ^1H-^1H correlation spectra (SI, Sections 8 and 9).

6. Comparison of α-δ $FAPbI_3$ phase transition kinetics for different particle sizes

For different distributions of particle sizes, the kinetics of α→δ $FAPbI_3$ in the presence of water vapor (85% RH) and laboratory illumination are presented in **Figure S8**. For large particles (40-100 micrometers), water vapor accelerates α→δ $FAPbI_3$ transformation during the early state of hydration, having one-half of the material converted to δ-$FAPbI_3$ phase within 15h, which increases to over 90% in less than two days; however, the rest of the transformation takes much longer exposure time. This is consistent with the optical microscopy analysis, which showed the sluggish transformation of the small cubic phase entrapped in the sub-surface layers of the hexagonal $FAPbI_3$ particles. Therefore, a complete α→δ $FAPbI_3$ transformation is expected to take up to a week or longer. The kinetics plots enabled by ^{1}H MAS analysis are particularly useful to estimate the half-life times for different particle sizes, which are presented in **Table S1**.

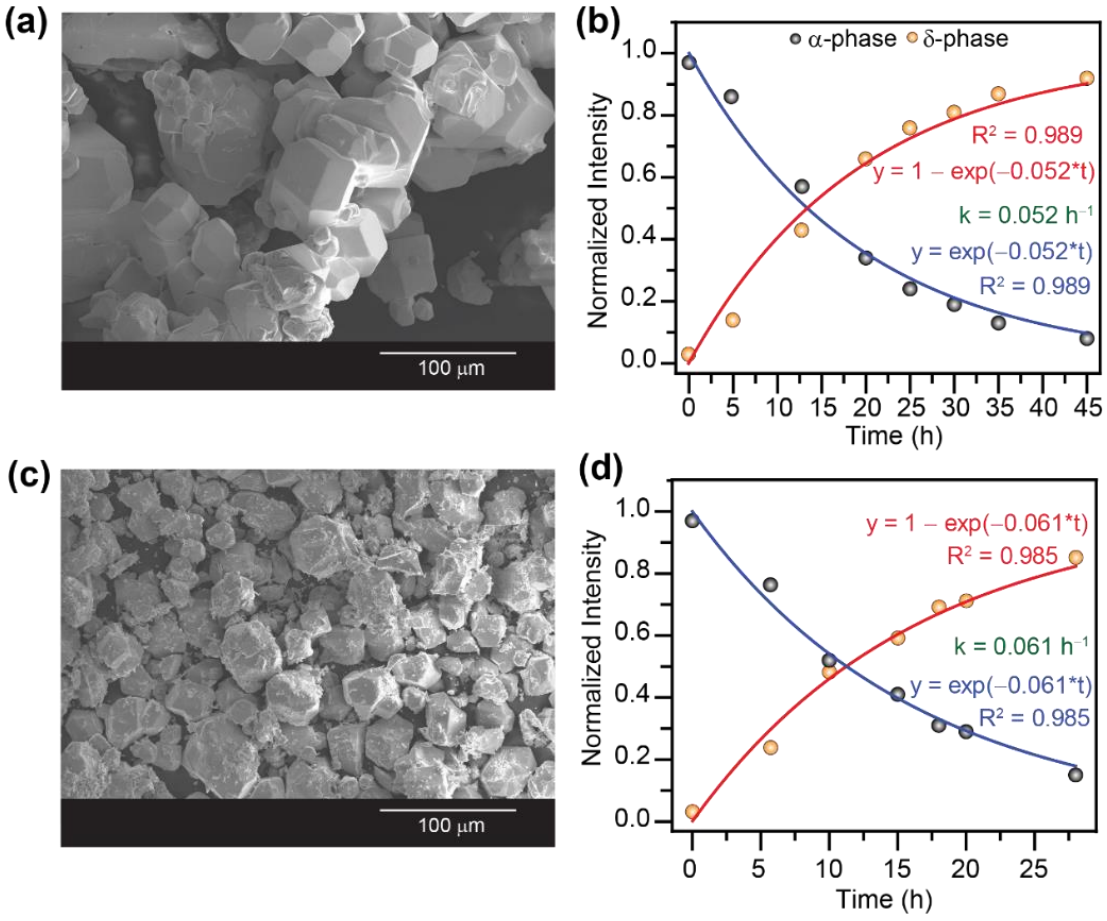

Figure S8. SEM micrographs of (a) large (74 μm) and (c) small (32 μm) particles. Normalized ^{1}H (-CH) signal intensities of FA cations in α and δ $FAPbI_3$ phases plotted as functions of moisture exposure time for (b) large and (d) small particles, depicting the kinetics of phase transformation in large and small $FAPbI_3$ particles. The rate constants and half-lives are shown in the figure insets.

Table S1. Half-life decay times of black $FAPbI_3$ crystals upon exposure to moisture at 85% RH.

Particle size	Half-life time ($t_{½}$, h)
Large (≈74 μm)	13.3
Small (≈32 μm)	11.4

For particles sizes in the range of 20-40 μm exposed to moisture (85% RH), the phase transformation studied by ^{1}H MAS NMR experiments shows the identical trend, whereby the rate of reaction is relatively faster during the early hydration period. After exposure to moisture for 15h, the phase transformation proceeds with a relatively lower rate because the black particles trapped in the yellow crystals are sparsely in contact with water molecules. These results suggest that the phase transformation follows the same pathway, but the kinetic rate depends on grain sizes. This is due to the large surface area associated with the corner-shared lead octahedra in the black phase being available to interact with molecules. For different distributions of particle sizes, the estimated half-lives are given in **Table S1**, and their kinetic plots are shown in **Figure S9**. Subtilities in the half-lives $\Delta t_{½}$ ~2h and rate constants Δk ~0.01 h^{-1} are observed, due to the partial overlap in the particle size distributions (see **Figure S3**). To accurately calculate the half-lives of different particle sizes, kinetics studies of particles with uniform size and shape are required. We note that the mere extrapolation of these kinetics plots to estimate the stability of $FAPbI_3$ thin films used in solar cells and other optoelectronic devices is less straightforward, because the thin film stability depends on the surface and interfacial passivation techniques and encapsulation strategies,[26–35] which requires further analysis at different humidity points and different grain sizes with and without passivating agents. However, the large grains benefit from the enhanced stability.

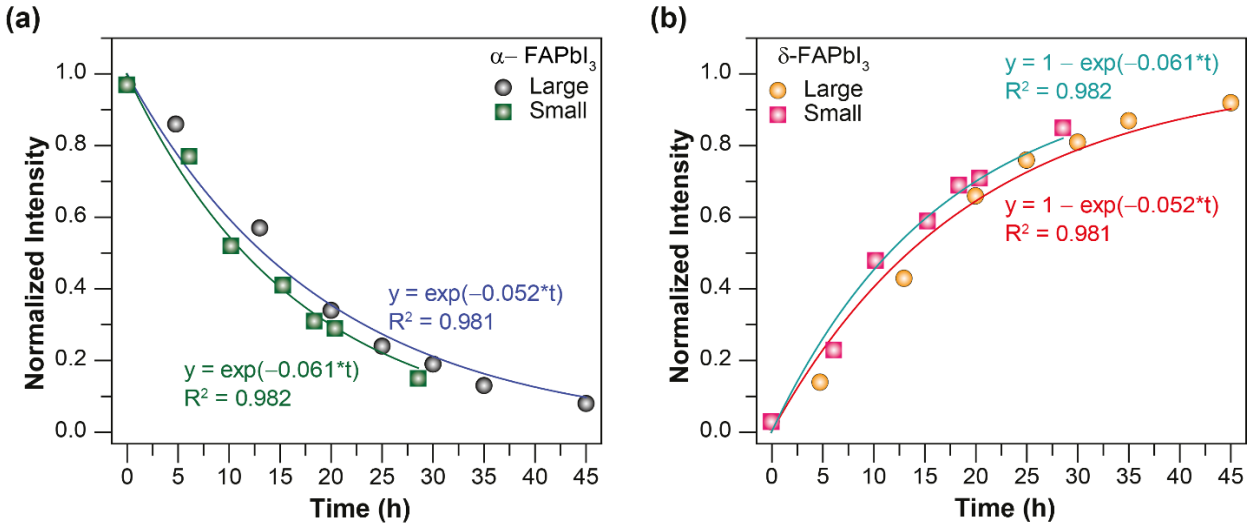

Figure S9. Comparison of (a) α– and (b) δ–$FAPbI_3$ phase transformation kinetics by means of ^{1}H signal intensity build-up and decay of -CH sites for small (20-40 μm, squares) and large (40-100 μm, dots) particles.

7. Impact of light illumination on the moisture stability of α–$FAPbI_3$

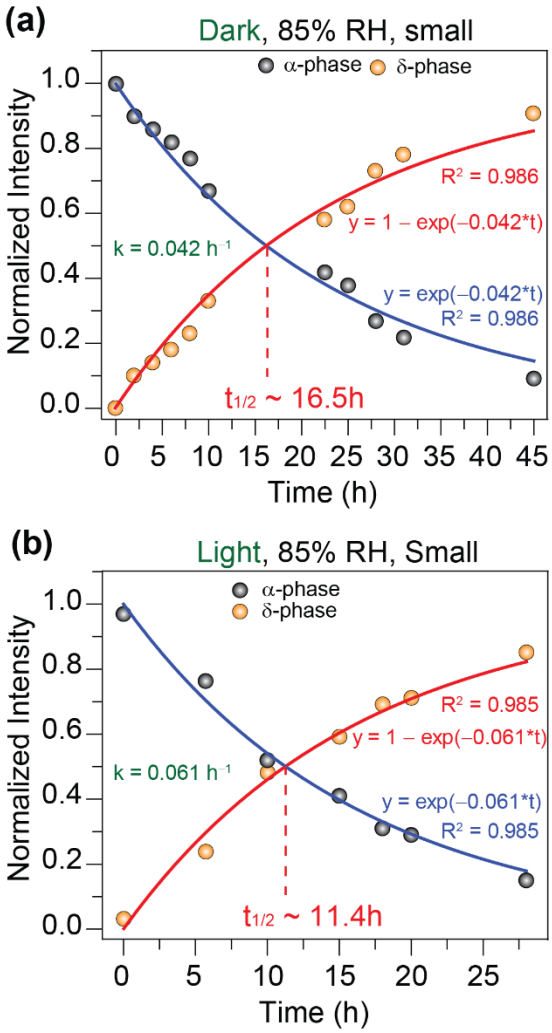

Figure S10. Kinetics plots of ^1H signal intensity buildup of -CH sites associated with δ–$FAPbI_3$ and the simultaneous ^1H signal intensity loss of the same sites in α–$FAPbI_3$ as a function of exposure time at 85% RH (a) in the absence and (b) presence of laboratory illumination. The phase transformation kinetics can be modeled to first-order rate kinetics, leading to the estimation of rate constants. For kinetic studies, smaller particles α–$FAPbI_3$ ≈32 μm were used.

Table S2. Half-lives ($t_{½}$) associated with α→δ $FAPbI_3$ phase transformation at 85% RH (smaller particles, 20-40 μm), in the presence and absence of light illumination.

Light illumination	Half-life decay time ($t_{½}$, h)
No	16.5
Yes	11.4

8. 2D ^{1}H-^{1}H DQ-SQ correlation NMR spectra of fresh and aged $FAPbI_3$

The 2D ^{1}H-^{1}H DQ-SQ correlation NMR experiment provides information on through-space and dipolar coupled ^{1}H-^{1}H spin pairs within sub-nanometer (5 Å) distances. In a 2D DQ-SQ correlation spectrum, the DQ frequencies are detected at the cumulative sum of the participating SQ frequencies of the dipolar coupled ^{1}H-^{1}H spin pairs. The DQ signals associated with chemically equivalent and dipole-dipole coupled ^{1}H-^{1}H pairs lead to the on-diagonal peaks, whereas chemically inequivalent ^{1}H-^{1}H pairs contribute to the off-diagonal signals. The enhanced resolution in the DQ dimension enables distinguishing and identifying the $–NH_2$ and –CH sites in α- and δ-$FAPbI_3$ phases. **Figure S11** shows the 2D ^{1}H-^{1}H DQ-SQ correlation NMR spectra of α-$FAPbI_3$, α|δ-$FAPbI_3$, and δ-$FAPbI_3$. For the fresh $FAPbI_3$ **(Figure S11a)**, the on-diagonal signal at 7.4 + 7.4 = 14.8 ppm corresponds to ^{1}H-^{1}H interactions in NH_2 groups of α-$FAPbI_3$, and off-diagonal ^{1}H DQ signal at 8.2 + 7.4 = 15.6 ppm is attributed to intramolecular CH↔NH_2 dipole-dipole interactions in the same material. The intermolecular and intramolecular CH↔NH_3 distances in the refined α-$FAPbI_3$ crystal structure are ≈4.54 Å and ≈2.28 Å, such that both inter- and intramolecular ^{1}H-^{1}H dipole-dipole interactions are expected to contribute to the off-diagonal signal.[10] However, the on-diagonal DQ signal associated with –CH sites at 8.2 + 8.2 = 16.4 ppm is too weak to be detected due to fast reorientational dynamics of FA^+ cations in the cubic phase.

For an intermediate α|δ-$FAPbI_3$ phase (**Figure S11b)**, two sets of DQ-SQ correlation peaks are detected. In addition to the above discussed 2D correlation peaks associated with the cubic phase, a partially resolved ^{1}H DQ peak at 7.6 + 7.6 = 15.2 ppm and an additional DQ signal at 7.6 + 8.6 = 16.2 ppm corresponding to the intramolecular proximity between $–NH_2$ and –CH proton sites in the hexagonal $FAPbI_3$ phase are observed. It is noteworthy that there is no ^{1}H DQ peak corresponding to the through-space proximity between the ^{1}H sites in the cubic and hexagonal phases. These results suggest that these FA^+ cations in α and δ–$FAPbI_3$ materials are spatially phase segregated into different regions. This is consistent with the optical microscopy data that showed heterogeneous interfaces between the black and yellow regions of $FAPbI_3$ particles. In addition, the cations exhibit different dynamics and reorientational motions in the cubic and hexagonal phases that may partially, or completely, average out the dipole-dipole couplings between the FA^+ cations in these two phases, thus contributing to the loss of ^{1}H DQ signal intensity.

Upon further exposure to moisture (85% RH, 35h), only the ^{1}H DQ signals corresponding to the yellow phase are observed (**Figure S11c)**, whereby the on-diagonal signal at 7.6 + 7.6 = 15.2 ppm and 8.6 + 8.6 = 17.2 ppm arises due to proximate $–NH_2$ and –CH protons, respectively. In addition, an off-diagonal DQ signal at 7.6 + 8.6 = 16.2 ppm corresponding to the intramolecular CH↔NH_2 dipolar interactions in δ-$FAPbI_3$ is observed.

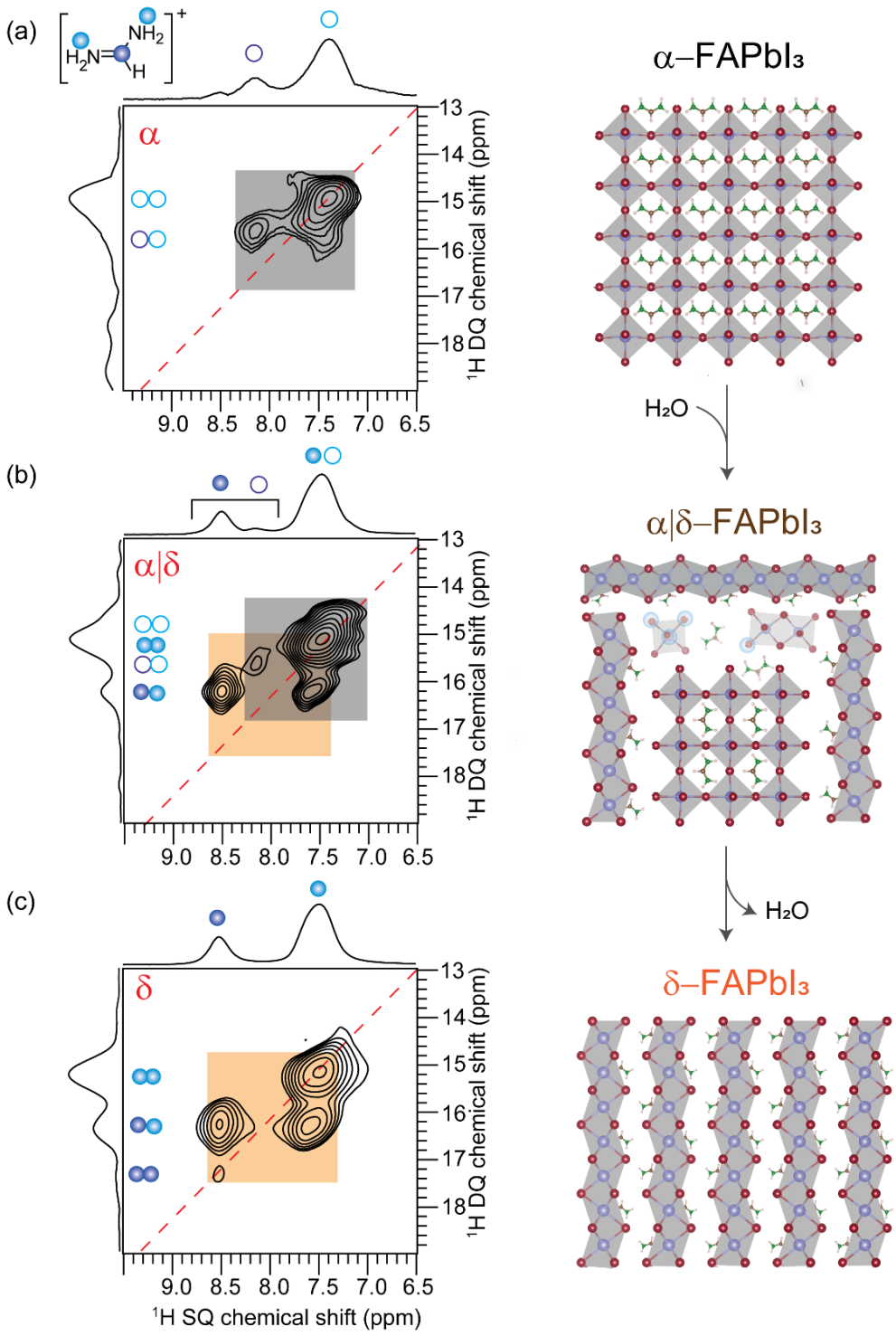

Figure S11. Solid-state 2D ^{1}H-^{1}H DQ-SQ correlation NMR spectra of (a) cubic (α)$FAPbI_3$, (b) partially transformed α|δ–$FAPbI_3$, and (c) δ–$FAPbI_3$ materials acquired at 21 T (^{1}H, 900.2 MHz) and at 50 kHz MAS frequency. Signals corresponding to –CH and $–NH_2$ are color-coded as depicted in the figure inset of (a).

9. 2D ^{1}H-^{1}H spin-diffusion NMR spectra of fresh and aged α–$FAPbI_3$

Analysis of 2D ^{1}H-^{1}H spin-diffusion NMR provides further insight into the spatial distribution of α– and δ–$FAPbI_3$ phases. In a 2D ^{1}H spin diffusion experiment, the ^{1}H magnetization is allowed to exchange between dipole-dipole coupled ^{1}H-^{1}H sites. At a shorter mixing time, the magnetization exchange occurs between closely proximate protons, whereas longer mixing times enable the magnetization exchange to occur between the distant proton sites mediated through a network of dipolar coupled protons. It is noteworthy that these experiments extend the ssNMR length scales from sub-nanometer to up to a few hundreds of nanometers in rigid systems.

Figure S12 shows the 2D ^{1}H-^{1}H spin-diffusion NMR spectra of α-$FAPbI_3$, α|δ $FAPbI_3$, and δ-$FAPbI_3$ with 1 ms and 200 ms. In a 2D ^{1}H-^{1}H spin-diffusion spectra acquired with τ_{mix} = 1 ms (**Figure S12a-c**), only diagonal peaks are observed that are identical to the signals in the 1D ^{1}H NMR spectrum, meaning this mixing time is not sufficient to allow magnetization exchange between the different proton sites to occur in $FAPbI_3$. In the 2D spectra acquired with τ_{mix} = 200 ms, off-diagonal peaks have emerged, which evidence the exchange of magnetization between different proton sites. The off-diagonal peaks in **Figure S12d-f** are attributable to spin magnetization exchange between –CH and $–(NH_2)_2$ sites in FA^+ cations within the α–$FAPbI_3$ and within the δ–$FAPbI_3$ phase. However, the off-diagonal peaks between –CH (α-$FAPbI_3$) and –CH (δ-$FAPbI_3$) are not detected even at longer mixing times (**Figure S12e**, τ_{mix} = 200 ms), indicating that there is no ^{1}H spin magnetization exchange between FA^+ cations in the black and yellow phases. These results corroborate the ^{1}H DQ-SQ measurements and analysis of black, intermediate, and yellow phases and optical microscopy results that showed heterogeneous interfaces between the black and yellow regions of $FAPbI_3$ upon exposure to moisture. These results further suggest that the plausible liquid-like interface between the black and yellow phase at the grain or sub-grain boundaries caused by surface wetting that leads to a (pseudo)first-order reaction kinetics, rather than a solid-to-solid transformation.

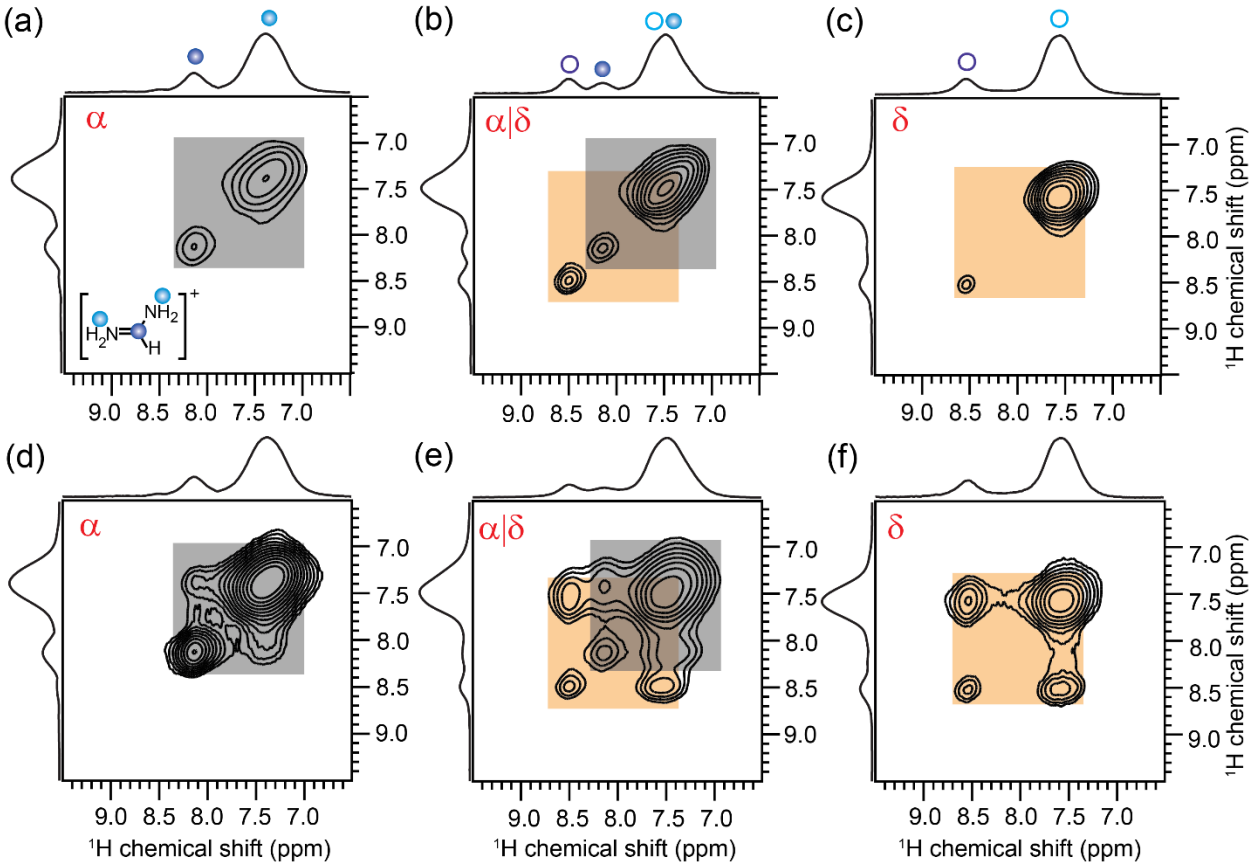

Figure S12. Solid-state 2D ^{1}H-^{1}H spin-diffusion NMR spectra of (a,d) fresh and aged (b,c,e,f) $FAPbI_3$ materials acquired at 21 T (^{1}H 900.2 MHz) with 50 kHz MAS. Signals corresponding to –CH and $–NH_2$ sites are color-coded as depicted in the figure inset of (a). (a-c) are acquired with 1 ms of mixing time, and (d-f) are acquired with 200 ms of spin diffusion time.

10. ^{2}H NMR line shape analysis of control α–$FAPbBr_3$ and δ–$FAPbI_3$ samples

For control (neat α-$FAPbBr_3$ and δ-$FAPbI_3$) and target samples (α-$FAPbI_3$ before and after exposure to moisture), the lineshape analyses static 1D ^{2}H NMR spectra were carried out using the sola package included in Bruker Topspin 4.1.3. For control samples, the isotropic ^{2}H chemical shifts were measured by ^{2}H MAS experiments with 15 kHz MAS frequency. These isotropic chemicals, anisotropy (CSA), and peak intensities were convoluted to best match the experimental static ^{2}H NMR spectra of control samples. For α-$FAPbBr_3$, the lineshape analysis leads to the isotropic chemical shift was found to be 8.3 ppm, and the anisotropy of 66.4 Hz was introduced to convolute the lineshape. For the δ-$FAPbI_3$ phase, the chemical shift of 8.0 was introduced with a CSA of 2.9 kHz, and the quadrupolar coupling constants of 53 kHz (small splitting) and 81 kHz (large splitting), which were attributable to different local chemical environments of ND_2 sites attached to the same FA cations. Based on this knowledge of chemical shifts and quadrupolar coupling constants, ^{2}H NMR lineshape analysis of partially converted alpha/delta-$FAPbI_3$ was carried out. For the target sample α-$FAPbI_3$ (after exposure to moisture, 6h at 85% RH), the ^{2}H line shape is convoluted with an isotropic chemical shift of 7.4 ppm and anisotropy of 12.0 ppm. Overall, the residual quadrupolar interactions may remain in this spectrum, which are negligible compared to the peak widths. For the sample α-$FAPbI_3$ after exposure to moisture (for 68h at 85% RH), the ^{2}H NMR exhibited a remarkably different lineshape that can be fitted into three different components; the narrow peak at ~7.7 ppm is attributed to the ND_2 sites in α-$FAPbI_3$, and the two distinct splitting with interpeak separation of 39.2 and 59.5 kHz are attributable to the different local chemical environments of ND_2 sites in δ-$FAPbI_3$ that are expected to exhibit different dynamic behaviors. The quadrupolar coupling constants are obtained from the lineshape fitting analysis were found to be 53 kHz for the small splitting and 81 kHz for large splitting.

This study employs ^{2}H NMR spectroscopy lineshape analysis and quadrupolar splitting to gain insight into the dynamics aspects of the FA^+ cations such as fast and slow reorientational motions, which occur at much faster timescales (fs-ps) compared to the $^1H \leftrightarrow ^2H$ isotopic exchange process that occurs at much slower time scales seconds to several hours, (*vide infra*).[36,37]

11. ^{1}H NMR spectra of α–FAPbI$_3$ treated with D$_2$O vapor (85% RH)

Pristine α–FAPbI$_3$ material was placed in a chamber with controlled (85% RH) D$_2$O exposure. Upon exposure to D$_2$O, we observe the formation of a α|δ–FAPbI$_3$ phase in 1D ^{1}H NMR spectra, as shown in **Figure S13.** Upon prolonged exposure to D$_2$O (68 h), signals corresponding to δ–FAPbI$_3$ are well-resolved. Signal deconvolution of the 1D ^{1}H NMR spectrum can provide insights into the level of deuteration. Knowing the chemical shift from 1D ^{1}H and 2D ^{1}H-^{1}H NMR experiments corresponding to distinct sites in α– and δ–FAPbI$_3$, signal deconvolution is more reliable. Each of the spectra in **Figure S13** was deconvoluted to estimate the extent of deuteration as a function of moisture exposure (D$_2$O) time.

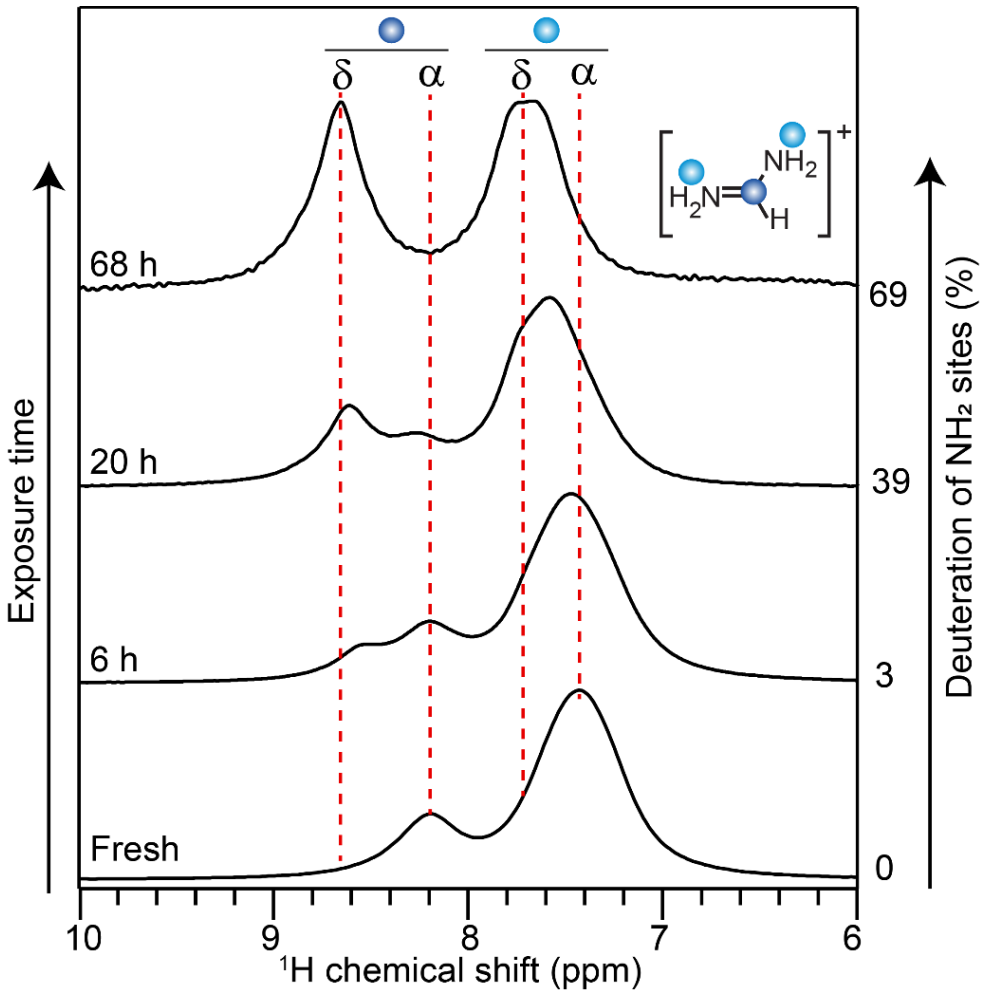

Figure S13. 1D ^{1}H MAS NMR spectra indicating the α–δ FAPbI$_3$ transformation upon exposure to D$_2$O at 85% RH. Signal intensity loss associated with NH$_2$ sites (7-8 ppm) indicates the on-the-fly deuteration of NH$_2$ sites of FA^{+} cations.

Starting from the fresh α-$FAPbI_3$, a 20 h of exposure to moisture (D_2O) yields nearly 39% of deuterated FA^+ cations, and prolonged exposure of up to 3 days leads to 69% of the FA^+ cations deuterated (α|δ $FAPbI_3$). **Figure S14** presents the deconvolution analysis of α|δ–$FAPbI_3$ phase after exposure to D_2O for 68 h. For the undertreated sample, as for every CH proton, there are four NH_2 protons present in the FA^+ cation. Therefore, the integral values of the ammonium sites versus the methylene sites in α– and δ–$FAPbI_3$ was 1:4. Upon exposure to D_2O, the NH_2 sites get deuterated. In the deuterated samples, the extent of deuteration was then evaluated by considering the difference in the integral values between CH and NH_2 protons. This analysis indicates that ~69% of the NH_2 sites are deuterated.

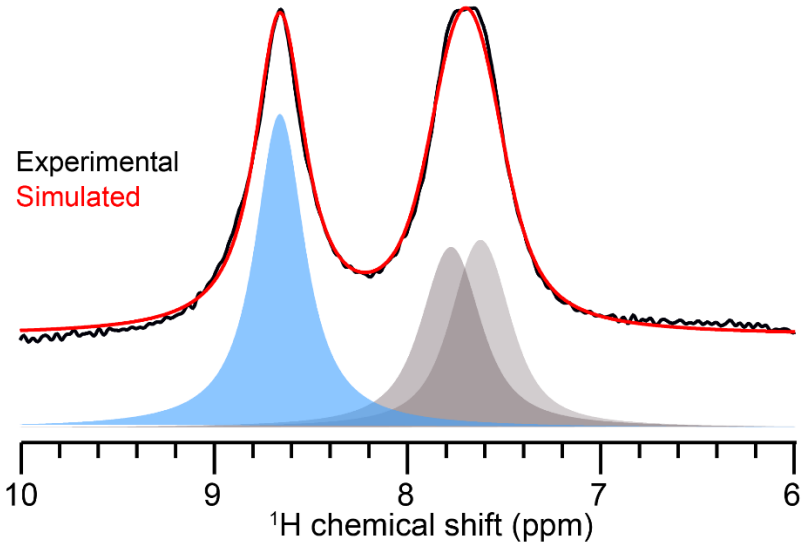

Figure S14. Line shape deconvolution analysis of a 1D ^1H MAS NMR spectrum of δ-$FAPbI_3$ after exposure to D_2O at 85% RH for 70h. Deconvolution analysis suggests that ~70% of NH_2 sites are deuterated as indicated by the signal intensity loss of NH_2 sites in the 7-8 ppm region because ND_2 sites do not contribute to the ^1H signal intensity.

By comparison, starting from the neat δ-$FAPbI_3$ as a control sample, 22h of exposure to moisture (D_2O) results in ~15% of the deuterated NH_2 sites, which upon further exposure to moisture (D_2O) for 48h leads to ~33% of deuterated NH_2 sites in FA^+ cations. **Figure S15** compares the lineshape analysis of ^2H (static and MAS) and ^1H MAS 48h exposed (D_2O) δ–$FAPbI_3$ material. This suggests that the $^1H \leftrightarrow ^2H$ isotopic exchange rate depends on the local chemical environment of FA^+ cations in alpha and delta phases, and calls for further investigation of isotopic exchange rates. As indicated above, ^2H lineshape analysis presented in this study is more suitable to understand the dynamics aspects and is less suited to study reaction kinetics.

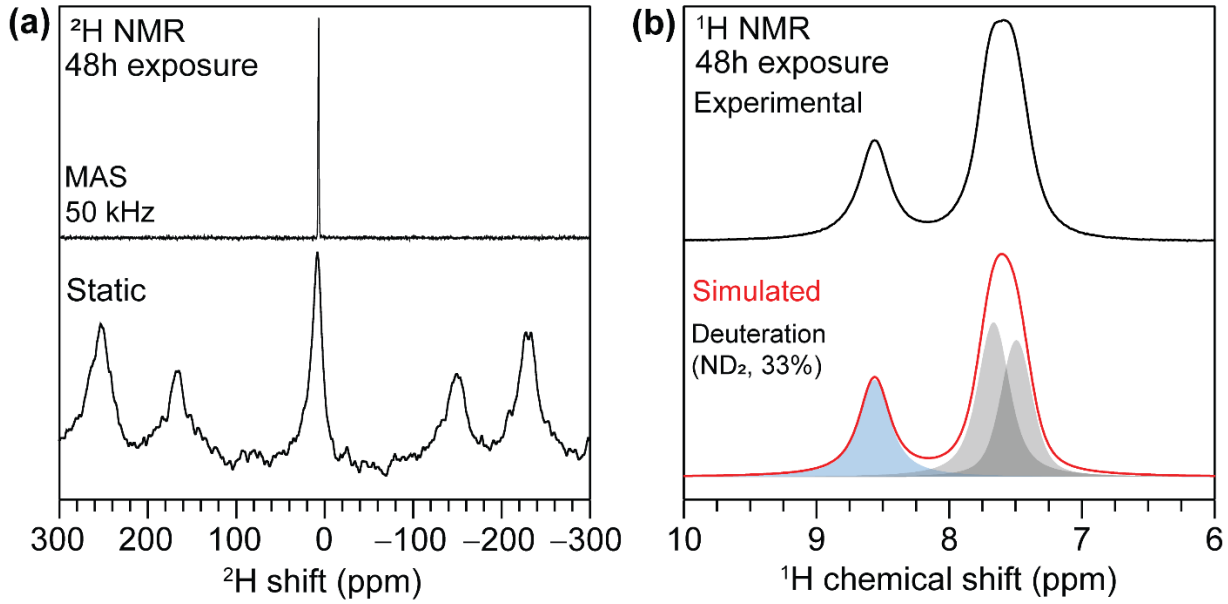

Figure S15. Solid-state 1D (a) static (bottom) and MAS (top) ^2H NMR and (b) ^1H MAS NMR spectra of $FAPbI_3$ acquired after exposure to D_2O for 48h (top) and its line shape deconvolution analysis (bottom) suggesting 33% of deuteration as indicated by the signal intensity loss of NH_2 sites in the 7-8 ppm region because ND_2 sites do not contribute to the ^1H signal intensity.

To summarize, it has been feasible to characterize the local structures of lead octahedra and organic cations in the kinetically trapped intermediate α|δ-$FAPbI_3$ phase at the atomic-level through 1D and 2D solid-state NMR spectroscopy techniques. Notably, ^2H quadrupolar splitting and ^1H and ^{207}Pb NMR shifts are sensitive to subtle changes at the organic-inorganic interface, hydrogen-bonding interactions between organic cations and lead iodide octahedra, and octahedral distortions. This study also corroborates that the phase transitions occur at the grain boundaries, whereby the black and yellow $FAPbI_3$ phases are phases segregated (see optical microscopy analysis, **Section 4**), as well as at the nanoscopic domains examined by 2D ^1H spin diffusion NMR analysis. Therefore, at the outer and inner layers of the same particle α–$FAPbI_3$ particles exhibit different phase transformations kinetics, leading to non-linear kinetic behavior. By comparison, $FAPbBr_3$ perovskites exhibited enhanced ambient stability under a wide range of humidity levels and exposure times (see 1D ^2H and 2D ^1H DQ-SQ spectra, **Figures S16 and S17**).

12. 1D ^{2}H and ^{1}H NMR spectra of $FAPbBr_3$ after exposure to D_2O (85% RH)

Figure S16 compares the static 1D ^{2}H NMR and ^{1}H MAS NMR spectra of $FAPbBr_3$ acquired after exposing the material to D_2O vapor for a period of 24 hours. The 1D static ^{2}H NMR spectrum **(Figure S16a)** shows a signal centered at 7.7 ppm attributed to the -ND_2 sites in $FAPbBr_3$, and a ^{2}H MAS NMR spectrum a narrow signal as the anisotropic contributions are averaged out, leading to an accurate measurement of the isotropic ^{2}H NMR chemical shift. As discussed in **section 9**, deconvolution analysis of the 1D ^{1}H MAS NMR spectrum (**Figure S16b**) has been used to determine the extent of deuteration. The extent of deuteration was examined by measuring and comparing the peak integral values for NH_2 and CH sites of FA^+ cations. Based on this analysis, we estimate that 33% of -NH_2 sites of $FAPbBr_3$ are deuterated upon exposure to D_2O for 48 h.

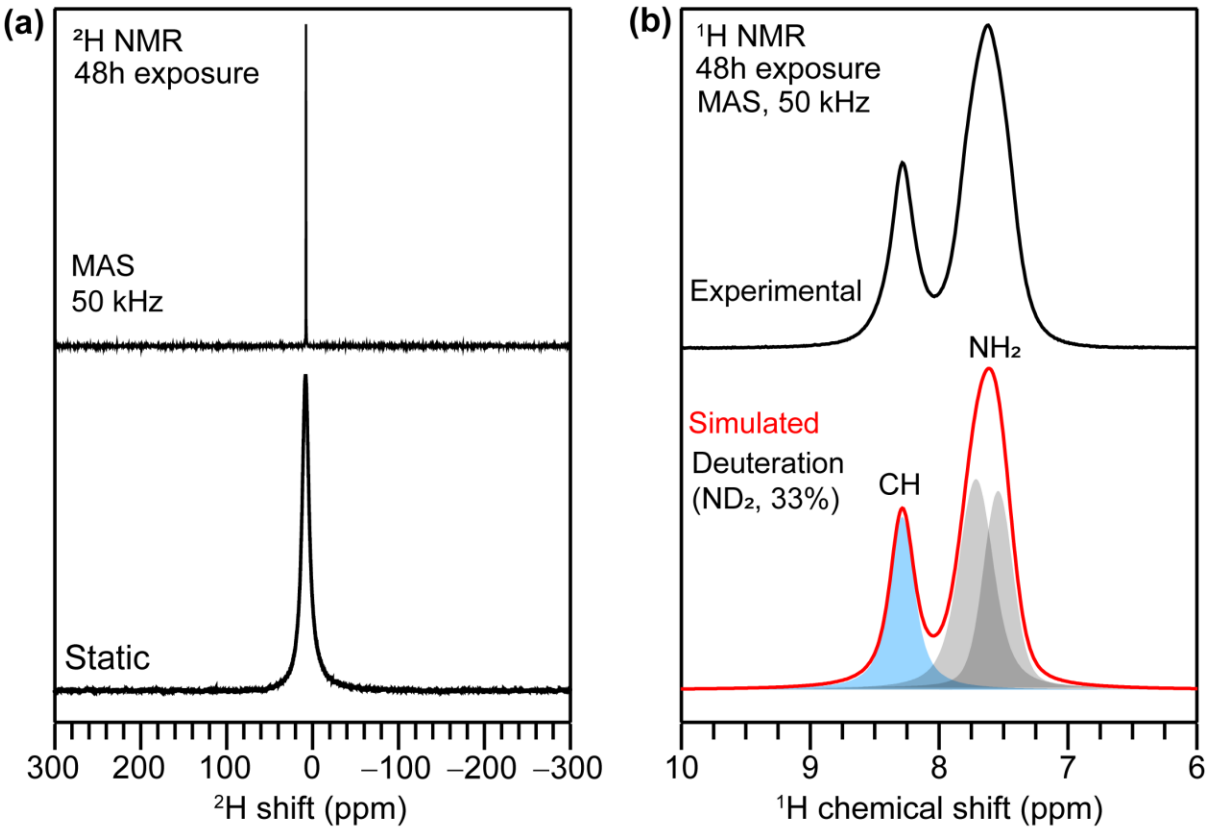

Figure S16. Solid-state 1D (a) ^{2}H NMR spectra recorded at static (bottom) and MAS (top), and (b) ^{1}H MAS NMR spectra of $FAPbBr_3$ acquired after exposure to D_2O for 48h (top) and its lineshape deconvolution analysis (bottom), suggesting 33% of deuteration of NH_2 sites.

13. 2D ^{1}H-^{1}H DQ-SQ correlation NMR spectra of $FAPbBr_3$ before and after exposure to moisture

Figure S17 shows the 2D ^{1}H-^{1}H DQ-SQ correlation NMR spectra of fresh and aged $FAPbBr_3$. For the fresh $FAPbBr_3$ **(Figure S17a)**, the on-diagonal signal at 7.6 + 7.6 = 15.2 ppm corresponds to ^{1}H-^{1}H interactions in NH_2 groups of $FAPbBr_3$, and off-diagonal ^{1}H DQ signal at 8.3 + 7.6 = 15.9 ppm is attributed to intramolecular $CH \leftrightarrow NH_2$ dipole-dipole interactions in the same material. Moreover, the on-diagonal DQ signal associated with –CH sites at 8.3 + 8.3 = 16.6 ppm is observed, unlike in the case of $FAPbI_3$, where the same signal was too weak to be detected due to fast reorientational dynamics of FA^+ cations in the cubic phase. Upon exposing this material to moisture (85% RH, 7 days), there are no significant changes observed in the 2D ^{1}H-^{1}H DQ-SQ correlation NMR spectrum of $FAPbBr_3$ as shown in **Figure S17b**.

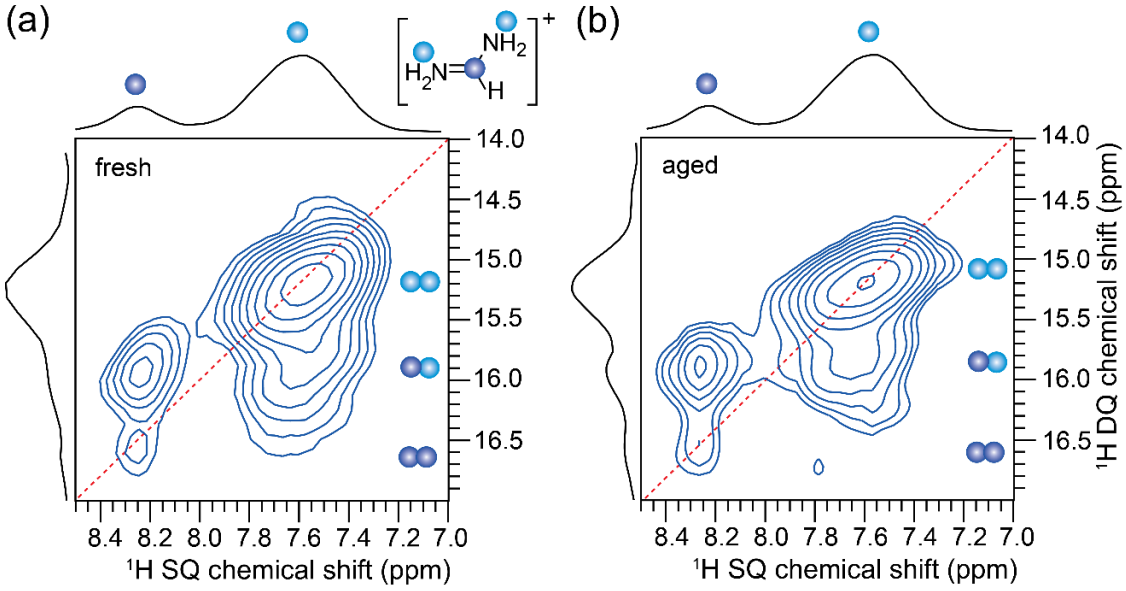

Figure S17. (a) Solid-state 2D ^{1}H-^{1}H DQ–SQ NMR correlation spectrum of fresh and aged (85 ± 5% RH, 7 days) $FAPbBr_3$ acquired at 20 T (^{1}H 900 MHz) and at 50 kHz MAS frequency. The corresponding skyline projections are shown along the top ^{1}H SQ horizontal and ^{1}H DQ vertical axes, respectively. Correlated signal intensities originating from dipolar-coupled ^{1}H-^{1}H pairs are depicted by colored circles.

14. References

(1) Spanopoulos, I.; Ke, W.; Stoumpos, C. C.; Schueller, E. C.; Kontsevoi, O. Y.; Seshadri, R.; Kanatzidis, M. G. Unraveling the Chemical Nature of the 3D "Hollow" Hybrid Halide Perovskites. *J. Am. Chem. Soc.* **2018**, *140*, 5728–5742.

(2) Schnell, I.; Lupulescu, A.; Hafner, S.; Demco, D. E.; Spiess, H. W. Resolution Enhancement in Multiple-Quantum MAS NMR Spectroscopy. *J. Magn. Reson.* **1998**, *133*, 61–69.

(3) Manjunatha Reddy, G. N.; Malon, M.; Marsh, A.; Nishiyama, Y.; Brown, S. P. Fast Magic-Angle Spinning Three-Dimensional Nmr Experiment for Simultaneously Probing H-H and N-H Proximities in Solids. *Anal. Chem.* **2016**, *88*, 11412–11419.

(4) Sommer, W.; Gottwald, J.; Demco, D. E.; Spiess, H. W. Dipolar Heteronuclear Multiple-Quantum NMR Spectroscopy in Rotating Solids. *J. Magn. Reson. Ser. A* **1995**, *113*, 131–134.

(5) Elena, B.; Emsley, L. Powder Crystallography by Proton Solid-State NMR Spectroscopy. *J. Am. Chem. Soc.* **2005**, *127*, 9140–9146.

(6) Elena, B.; Pintacuda, G.; Mifsud, N.; Emsley, L. Molecular Structure Determination in Powders by NMR Crystallography from Proton Spin Diffusion. *J. Am. Chem. Soc.* **2006**, *128*, 9555–9560.

(7) Hanrahan, M. P.; Men, L.; Rosales, B. A.; Vela, J.; Rossini, A. J. Sensitivity-Enhanced ^{207}Pb Solid-State NMR Spectroscopy for the Rapid, Non-Destructive Characterization of Organolead Halide Perovskites. *Chem. Mater.* **2018**, *30*, 7005–7015.

(8) Lee, J.; Lee, W.; Kang, K.; Lee, T.; Lee, S. K. Layer-by-Layer Structural Identification of 2D Ruddlesden–Popper Hybrid Lead Iodide Perovskites by Solid-State NMR Spectroscopy. *Chem. Mater.* **2021**, *33*, 370–377.

(9) Harris, R. K.; Becker, E. D.; Cabral De Menezes, S. M.; Goodfellow, R.; Granger, P. NMR Nomenclature. Nuclear Spin Properties and Conventions for Chemical Shifts(IUPAC Recommendations 2001). *Pure Appl. Chem.* **2001**, *73*, 1795–1818.

(10) Weller, M. T.; Weber, O. J.; Frost, J. M.; Walsh, A. Cubic Perovskite Structure of Black Formamidinium Lead Iodide, α-$[HC(NH_2)_2]PbI_3$, at 298 K. *J. Phys. Chem. Lett.* **2015**, *6*, 3209–3212.

(11) Stoumpos, C. C.; Malliakas, C. D.; Kanatzidis, M. G. Semiconducting Tin and Lead Iodide Perovskites with Organic Cations: Phase Transitions, High Mobilities, and near-Infrared Photoluminescent Properties. *Inorg. Chem.* **2013**, *52*, 9019–9038.

(12) Macrae, C. F.; Sovago, I.; Cottrell, S. J.; Galek, P. T. A.; McCabe, P.; Pidcock, E.; Platings, M.; Shields, G. P.; Stevens, J. S.; Towler, M.; Wood, P. A. Mercury 4.0: From Visualization to Analysis, Design and Prediction. *J. Appl. Crystallogr.* **2020**, *53*, 226–235.

(13) Li, W.; Rothmann, M. U.; Zhu, Y.; Chen, W.; Yang, C.; Yuan, Y.; Choo, Y. Y.; Wen, X.; Cheng, Y. B.; Bach, U.; Etheridge, J. The Critical Role of Composition-Dependent Intragrain Planar Defects in the Performance of $MA_{1-x}FA_xPbI_3$ Perovskite Solar Cells. *Nat. Energy* **2021**, *6*, 624–632.

(14) Rothmann, M. U.; Li, W.; Zhu, Y.; Bach, U.; Spiccia, L.; Etheridge, J.; Cheng, Y. B. Direct

Observation of Intrinsic Twin Domains in Tetragonal $CH_3NH_3PbI_3$. *Nat. Commun.* **2017**, *8*, 14547.

(15) Kennard, R. M.; Dahlman, C. J.; Decrescent, R. A.; Schuller, J. A.; Mukherjee, K.; Seshadri, R.; Chabinyc, M. L. Ferroelastic Hysteresis in Thin Films of Methylammonium Lead Iodide. *Chem. Mater.* **2021**, *33*, 298–309.

(16) Mittemeijer, E. J. Analysis of the Kinetics of Phase Transformations. *J. Mater. Sci.* **1992**, *27*, 3977–3987.

(17) Rollett, A.; Humphreys, F.; Rohrer, G. S.; Hatherly, M. Recrystallization of Single-Phase Alloys. In *Recrystallization and Related Annealing Phenomena (Second Edition)*; Elsevier Ltd, 2004; pp 215–267.

(18) Avrami, M. Granulation, Phase Change, and Microstructure Kinetics of Phase Change. III. *J. Chem. Phys.* **2004**, *9*, 177.

(19) Avrami, M. Kinetics of Phase Change. II Transformation-Time Relations for Random Distribution of Nuclei. *J. Chem. Phys.* **2004**, *8*, 212.

(20) Avrami, M. Kinetics of Phase Change. I General Theory. *J. Chem. Phys.* **2004**, *7*, 1103.

(21) Jena, A. K.; Chaturvedi, M. C. *Phase Transformation in Materials*; Prentice Hall, 1992.

(22) Khawam, A.; Flanagan, D. R. Solid-State Kinetic Models: Basics and Mathematical Fundamentals. *J. Phys. Chem. B* **2006**, *110*, 17315–17328.

(23) Pérez-Maqueda, L. A.; Criado, J. M.; Sánchez-Jiménez, P. E. Combined Kinetic Analysis of Solid-State Reactions: A Powerful Tool for the Simultaneous Determination of Kinetic Parameters and the Kinetic Model without Previous Assumptions on the Reaction Mechanism. *J. Phys. Chem. A* **2006**, *110*, 12456–12462.

(24) Segal, E. Rate Equations of Solid State Reactions. Euclidean and Fractal Models. *Rev. Roum. Chim.* **2012**, *57*, 491–493.

(25) Jander, W. Reaktionen Im Festen Zustande Bei Höheren Temperaturen. Reaktionsgeschwindigkeiten Endotherm Verlaufender Umsetzungen. *Zeitschrift für Anorg. und Allg. Chemie* **1927**, *163*, 1–30.

(26) Castro-Méndez, A. F.; Hidalgo, J.; Correa-Baena, J. P. The Role of Grain Boundaries in Perovskite Solar Cells. *Adv. Energy Mater.* **2019**, *9*, 1901489.

(27) Li, H.; Wu, G.; Li, W.; Zhang, Y.; Liu, Z.; Wang, D.; Liu, S.; Li, H.; Wu, G.; Li, W.; Liu, Z.; Wang, D.; Liu, S.; Zhang, Y. Additive Engineering to Grow Micron-Sized Grains for Stable High Efficiency Perovskite Solar Cells. *Adv. Sci.* **2019**, *6*, 1901241.

(28) Hu, M.; Bi, C.; Yuan, Y.; Bai, Y.; Huang, J.; Hu, M.; Bi, C.; Yuan, Y.; Bai, Y.; Huang, J. Stabilized Wide Bandgap $MAPbBr_xI_{3-x}$ Perovskite by Enhanced Grain Size and Improved Crystallinity. *Adv. Sci.* **2016**, *3*, 1500301.

(29) Wang, M.; Yin, Y.; Cai, W.; Liu, J.; Han, Y.; Feng, Y.; Dong, Q.; Wang, Y.; Bian, J.; Shi, Y. Synergetic Co-Modulation of Crystallization and Co-Passivation of Defects for $FAPbI_3$ Perovskite Solar Cells. *Adv. Funct. Mater.* **2022**, *32*, 2108567.

(30) Wang, Z.; Pradhan, A.; Kamarudin, M. A.; Pandey, M.; Pandey, S. S.; Zhang, P.; Ng, C. H.; Tripathi, A. S. M.; Ma, T.; Hayase, S. Passivation of Grain Boundary by Squaraine

Zwitterions for Defect Passivation and Efficient Perovskite Solar Cells. *ACS Appl. Mater. Interfaces* **2019**, *11*, 10012–10020.

(31) Kim, W.; Park, J. B.; Kim, H.; Kim, K.; Park, J.; Cho, S.; Lee, H.; Pak, Y.; Jung, G. Y. Enhanced Long-Term Stability of Perovskite Solar Cells by Passivating Grain Boundary with Polydimethylsiloxane (PDMS). *J. Mater. Chem. A* **2019**, *7*, 20832–20839.

(32) Ma, S.; Yuan, G.; Zhang, Y.; Yang, N.; Li, Y.; Chen, Q. Development of Encapsulation Strategies towards the Commercialization of Perovskite Solar Cells. *Energy Environ. Sci.* **2022**, *15*, 13–55.

(33) Mohammadi, M.; Gholipour, S.; Malekshahi Byranvand, M.; Abdi, Y.; Taghavinia, N.; Saliba, M. Encapsulation Strategies for Highly Stable Perovskite Solar Cells under Severe Stress Testing: Damp Heat, Freezing, and Outdoor Illumination Conditions. *ACS Appl. Mater. Interfaces* **2021**, *13*, 45455–45464.

(34) Zheng, X.; Chen, B.; Dai, J.; Fang, Y.; Bai, Y.; Lin, Y.; Wei, H.; Zeng, X. C.; Huang, J. Defect Passivation in Hybrid Perovskite Solar Cells Using Quaternary Ammonium Halide Anions and Cations. *Nat. Energy* **2017**, *2*, 17102.

(35) Alharbi, E. A.; Alyamani, A. Y.; Kubicki, D. J.; Uhl, A. R.; Walder, B. J.; Alanazi, A. Q.; Luo, J.; Burgos-Caminal, A.; Albadri, A.; Albrithen, H.; Alotaibi, M. H.; Moser, J. E.; Zakeeruddin, S. M.; Giordano, F.; Emsley, L.; Grätzel, M. Atomic-Level Passivation Mechanism of Ammonium Salts Enabling Highly Efficient Perovskite Solar Cells. *Nat. Commun.* **2019**, *10*, 3008.

(36) Hvidt, A. Deuterium Exchange between Ribonuclease and Water. *Biochim. Biophys. Acta* **1955**, *18*, 306–308.

(37) Masson, G. R.; Burke, J. E.; Ahn, N. G.; Anand, G. S.; Borchers, C.; Brier, S.; Bou-Assaf, G. M.; Engen, J. R.; Englander, S. W.; Faber, J.; Garlish, R.; Griffin, P. R.; Gross, M. L.; Guttman, M.; Hamuro, Y.; Heck, A. J. R.; Houde, D.; Iacob, R. E.; Jørgensen, T. J. D.; Kaltashov, I. A.; Klinman, J. P.; Konermann, L.; Man, P.; Mayne, L.; Pascal, B. D.; Reichmann, D.; Skehel, M.; Snijder, J.; Strutzenberg, T. S.; Underbakke, E. S.; Wagner, C.; Wales, T. E.; Walters, B. T.; Weis, D. D.; Wilson, D. J.; Wintrode, P. L.; Zhang, Z.; Zheng, J.; Schriemer, D. C.; Rand, K. D. Recommendations for Performing, Interpreting and Reporting Hydrogen Deuterium Exchange Mass Spectrometry (HDX-MS) Experiments. *Nat. Methods* **2019**, *16*, 595–602.